TURBULENCE STATISTICS IN WRF HYBRID LES MODEL FOR TEMPERATURE AND MOMENTUM

Kazim Sayeed *, **Clement Blervacq, Nicolas Massei, Luminita Danaila**
Morphodynamique Continentale et Côtière - UMR CNRS 6143 M2C,
Université de Rouen Normandie
Mont Saint Aignan, Rouen, France
* kazim-hussain-nasir.sayeed@univ-rouen.fr

ABSTRACT

Atmospheric extremes couple processes across a wide range of scales, from synoptic and mesoscale dynamics to boundary-layer turbulence and thermodynamic/radiative feedbacks. Quantifying how momentum and temperature variability are redistributed across scales is essential for both physical understanding and model evaluation. We analyse a seven-day simulation of the June 2019 European heatwave performed with the Weather Research and Forecasting (WRF) model (Skamarock *et al.*, 2019) in a hybrid Large-Eddy Simulation (LES) configuration with five one-way nested domains, spanning horizontal grid spacings from 15 km down to 67 m.

We diagnose second- and third-order structure functions of velocity and moist potential temperature, together with *scale-by-scale* (SBS) budget equations for the corresponding second-order moments. The SBS budgets are obtained in physical space by differencing the governing equations at two points and are evaluated directly from the resolved WRF fields and subgrid tendencies. The resulting balances isolate, as functions of separation r and height, the contributions of nonlinear transfer, large-scale advection/inhomogeneity, compressibility, pressure-related terms, subgrid transport and dissipation, Coriolis effects and a residual term that collects remaining model tendencies.

For the free-tropospheric diagnostics shown here (5 km altitude), the horizontal structure functions exhibit a near-Kolmogorov behaviour over a substantial range of separations, with a transition around the buoyancy/Ozmidov range inferred from independently estimated characteristic scales. At larger separations, the SBS budget highlights the dominant contribution of pressure-related terms and the emergence of rotational constraints near deformation/Rhines scales. Overall, the proposed SBS diagnostics provide a physically transparent route to connect WRF-resolved variability to the underlying dynamical balances across scales, and to identify scale ranges where model physics and external forcing most strongly imprint the statistics.

1 Introduction

Europe's June 2019 heatwave produced record-breaking near-surface temperatures, large impacts on health and infrastructure, and persistent atmospheric conditions favouring strong clear-sky radiative forcing and weak ventilation (Xu *et al.*, 2020). From a fluid-dynamical viewpoint, such events are intrinsically *multi-scale*: large-scale circulation and quasi-balanced dynamics set the background state, mesoscale organization controls coherent variability (jets, waves, fronts and convective patterns), and boundary-layer turbulence governs the near-surface exchange of momentum and heat.

Scale interactions in the atmosphere are often discussed in spectral space, where cascade phenomenology can be expressed through fluxes across wavenumbers. For nested numerical simulations over complex terrain, however, spectral tools are not always convenient: the domain is not periodic, statistics are spatially inhomogeneous, and the effective resolved range changes from one nest to the next. Physical-space diagnostics based on increments and structure functions provide a robust alternative because they can be evaluated locally, do not require periodicity, and can be coupled directly to the governing equations through exact two-point (scale-by-scale, SBS) budgets.

In this work we combine WRF hybrid-LES simulations with an SBS analysis of momentum and thermodynamic fields. Our objectives are: (i) to document velocity and scalar structure functions across nested domains spanning $\Delta x = 15$ km down to 67 m; (ii) to diagnose SBS budgets of second-order moments and identify which physical terms control the balance at each separation; and (iii) to relate regime transitions to independently estimated characteristic atmospheric length scales (buoyancy, Ozmidov, deformation and Rhines scales). The present TSFP contribution focuses on horizontal increments and free-tropospheric diagnostics (5 km altitude) as a representative example; the same framework applies at other heights and for conditional averages (day/night, pre-/peak-/post-heatwave).

2 Model configuration

We use the Advanced Research WRF (ARW) dynamical core in flux form with a terrain-following hybrid η coordinate and fully compressible, non-hydrostatic equations (Skamarock *et al.*, 2019). Turbulence closure is provided by the scale-adaptive three-dimensional TKE scheme (Zhang *et al.*, 2018), which supplies direction-dependent eddy viscosities applicable both in the planetary boundary layer (PBL) and in the stably stratified free troposphere. Radiative tendencies are computed with the Rapid Radiative Transfer Model for GCMs (RRTMG) (Iacono *et al.*, 2008). Surface exchange uses the revised MM5 scheme with Monin–Obukhov similarity (Jiménez *et al.*, 2012). Land-surface processes are represented by Noah-MP (Niu *et al.*, 2011), and cloud microphysics uses the Thompson bulk scheme (Thompson *et al.*, 2008).

A five-domain one-way nesting strategy spans horizontal

Domain	**Size** (km × km × km)	$\Delta x = \Delta y$	Δz
D00	$3600 \times 3450 \times 12$	15 km	10–250 m
D01	$880 \times 500 \times 12$	5 km	10–200 m
D02	$375 \times 140 \times 12$	1 km	10–200 m
D03	$70 \times 70 \times 12$	200 m	10–200 m
D04	$23 \times 23 \times 12$	67 m	5–100 m

Table 1. One-way nested model domain configurations. Domain labels D00–D04 are used consistently in the text and figure captions.

grid spacings from 15 km down to 67 m (table 1). Initial and lateral boundary conditions are prescribed from ERA5 reanalysis (Hersbach *et al.*, 2020) for the two outer nests, while inner nests are forced by their respective parent domains (figure 1). The simulation period extends from 23 June 2019, 12:00 UTC to 30 June 2019, 16:00 UTC and encompasses the peak of the heatwave episode analysed in (Xu *et al.*, 2020).

Unless otherwise stated, two-point statistics and SBS budgets are computed for separations confined to the horizontal plane, and averaged horizontally over interior points (to avoid boundary contamination) at fixed geometric heights above mean sea level. The results presented below correspond to 5 km altitude and time averages over the full simulation window, providing a first overview of free-tropospheric multi-scale balances during the event.

3 Methods: increments, structure functions and SBS budgets

3.1 Two-point notation and structure functions

For any resolved variable $a(\mathbf{x},t)$ we define the increment between two points $\mathbf{x}^{\pm} = \mathbf{X} \pm \mathbf{r}/2$ as

$$\delta a(\mathbf{X},\mathbf{r},t) = a(\mathbf{x}^+,t) - a(\mathbf{x}^-,t) \equiv a^+ - a^-, \qquad (1)$$

with midpoint $\mathbf{X} = (\mathbf{x}^+ + \mathbf{x}^-)/2$ and separation $\mathbf{r} = \mathbf{x}^+ - \mathbf{x}^-$. We consider separations confined to the horizontal plane, $\mathbf{r} = (r_x, r_y, 0)$, and report statistics as functions of $r = \|\mathbf{r}\|$. For velocity $\mathbf{u}$ we use the longitudinal increment $\delta u_\parallel = \delta \mathbf{u} \cdot \mathbf{r}/r$ and compute second- and third-order structure functions such as

$$S_2^u(r) = \langle (\delta u_i)^2 \rangle, \qquad S_3^u(r) = \langle \delta u_\parallel (\delta u_i)^2 \rangle, \qquad (2)$$

with analogous definitions for moist potential temperature θ_m. In the WRF outputs analysed here, θ_m denotes the model moist potential temperature diagnostic (i.e. potential temperature including moisture effects); we keep the generic notation θ_m for brevity.

Here $\langle \cdot \rangle$ denotes horizontal and temporal averaging at a prescribed height (unless stated otherwise). In contrast with Fourier spectra, these definitions do not require periodicity and can be applied consistently across nested domains.

3.2 Scale-by-scale kinetic-energy budget

By subtracting the governing momentum equations (see Göbel *et al.*, 2022) written at $\mathbf{x}^+$ and $\mathbf{x}^-$, multiplying by $2\,\delta u_i$, and rearranging in the $(\mathbf{X},\mathbf{r})$ coordinates, one obtains an exact SBS budget for the second-order velocity increments (see, e.g., Danaila *et al.*, 2012; Lindborg & Cho, 2001; Hill, 2001). In compact form, the WRF-resolved, SBS kinetic-energy budget becomes, viz.

$$\begin{aligned}
&\underbrace{\partial_t \langle (\delta u_i)^2 \rangle}_{\text{I (non-stationarity)}} + \underbrace{\partial_{r_j} \langle \delta u_j (\delta u_i)^2 \rangle}_{\text{II (scale transfer)}} \\
&+ \underbrace{\left\langle \frac{u_j^+ + u_j^-}{2}\, \partial_{X_j} (\delta u_i)^2 \right\rangle}_{\text{III (inhomogeneity)}} - \underbrace{\left\langle \frac{(\partial_j u_j)^+ + (\partial_j u_j)^-}{2}\, (\delta u_i)^2 \right\rangle}_{\text{IV (compressibility)}} \\
&= \underbrace{-2 \langle (\delta u_i)(\delta \alpha)\, \partial_{r_i} (\delta p) \rangle}_{T_{\text{V}}\text{ (pressure, }r\text{-divergence)}} + \underbrace{- \langle (\delta u_i)(\alpha^+ + \alpha^-)\, \partial_{X_i} (\delta p) \rangle}_{T_{\text{VI}}\text{ (pressure, inhomogeneity)}} \\
&+ \underbrace{\left\langle (K_j^+ + K_j^-)\, \partial_{r_j}^2 (\delta u_i)^2 \right\rangle}_{\text{VII (subgrid, }r\text{-divergence)}} + \underbrace{\left\langle \frac{(K_j^+ + K_j^-)}{4}\, \partial_{X_j}^2 (\delta u_i)^2 \right\rangle}_{\text{VIII (subgrid, inhomogeneity)}} \\
&+ \underbrace{\left\langle (K_j^+ - K_j^-)\, \partial_{r_j} \partial_{X_j} (\delta u_i)^2 \right\rangle}_{\text{IX (subgrid, mixed)}} - \underbrace{2\varepsilon_{\text{turb}}^+ - 2\varepsilon_{\text{turb}}^-}_{\text{X (subgrid dissipation/production)}} \\
&+ \underbrace{2 \langle \delta u_i\, \delta (f_{u_i,\text{coriolis}}) \rangle}_{\text{XI (Coriolis)}} + \underbrace{2 \langle \delta u_i\, \delta (f_{u_i,\text{residual}}) \rangle}_{\text{XII (residual)}}.
\end{aligned} \qquad (3)$$

For clarity, we define the signed pressure contributions T_{V} and T_{VI} as written on the right-hand side of (3), i.e. including the leading minus signs.

In (3), $\alpha = 1/\rho$, p is pressure, and K_j denotes the direction-dependent eddy viscosity supplied by the hybrid-LES closure (index j labels the coordinate direction). Term II is the r-space divergence of a third-order moment and represents scale-by-scale energy transfer in the horizontal plane. Terms III and VI–VIII quantify the effects of inhomogeneity and nesting-scale variability through derivatives with respect to $\mathbf{X}$.

3.3 Scalar budgets and diabatic sources

The same two-point procedure applies to prognostic scalars. For a generic scalar $\phi \in \{\theta_m, q_m\}$ with governing equation $\partial_t \phi + u_j \partial_j \phi = \mathscr{S}_\phi + \mathscr{D}_\phi$, where $\mathscr{S}_\phi$ denotes diabatic tendencies (radiation, microphysics, surface fluxes) and $\mathscr{D}_\phi$ subgrid diffusion, one obtains an SBS budget for $(\delta\phi)^2$ of the form

$$\begin{aligned}
\partial_t \langle (\delta\phi)^2 \rangle + \partial_{r_j} \langle (\delta u_j (\delta\phi)^2) \rangle + (\text{inhomogeneity/compressibility}) = \\
-2 \langle \delta\phi\, \delta\mathscr{S}_\phi \rangle + (\text{diffusion}) + (\text{residual}).
\end{aligned} \qquad (4)$$

This decomposition separates the purely advective cascade-like contribution (third-order moment) from the direct injection/removal of scalar variance by diabatic forcing.

3.4 Characteristic length scales

To interpret regime transitions in the structure functions and SBS budgets, we compare the separation r to independently estimated characteristic length scales (figure 2). We consider, among others, the Kolmogorov microscale $\eta = (\nu^3/\varepsilon)^{1/4}$, the Taylor microscale λ, the Ozmidov scale $L_O = (\varepsilon/N^3)^{1/2}$ (with Brunt–Väisälä frequency N), the buoyancy scale $L_B \sim U/N$, the Rhines scale $L_R \sim (U/\beta)^{1/2}$ and the

Rossby radius of deformation $L_D \sim NH/f$ (with Coriolis parameter f). These scales delineate ranges where stratification or rotation constrain the dynamics and where different scaling behaviours may emerge.

4 Results

4.1 Structure functions across domains

Figure 3 reports second- and third-order horizontal structure functions for the resolved velocity, and for the moist potential temperature at 5 km altitude, averaged over the full simulation period. The nested-domain configuration enables a continuous coverage of separations from the outer-domain mesoscale down to the LES-resolved range in the innermost nest. Over the mesoscale band between the buoyancy scale ($r \sim 10^4$ m) and the Rossby radius of deformation ($r \sim 10^6$ m), the velocity structure functions display steeper, non-Kolmogorov scalings: $S_2^u(r)$ is broadly consistent with $S_2^u(r) \propto r^{4/3}$ and $S_3^u(r)$ with $S_3^u(r) \propto r^2$ with steepness increasing in region where S_3^u switches sign. These exponents are also consistent with the best-fit slopes one can infer from Lindborg's free-tropospheric aircraft observations, even though those works do not highlight them explicitly (Lindborg & Cho, 2001; Cho & Lindborg, 2001). By contrast, near-Kolmogorov behaviour ($S_2^u(r) \sim r^{2/3}$ and $S_3^u(r) \sim r$) is only apparent over a comparatively narrow interval just below the buoyancy scale, before subgrid/numerical effects at smaller separations begin to dominate and steepen the apparent slopes.

At the largest separations, the structure functions depart from simple power laws and reflect the imprint of coherent mesoscale organization, large-scale gradients and rotational constraints. Taken together, these features are consistent with the expectation that stratification and rotation constrain the largest eddies, while smaller separations progressively recover more local transfer behaviour.

The scalar second-order structure function $S_2^\theta(r) = \langle(\delta\theta_m)^2\rangle$ exhibits similar multi-regime behaviour, but with stronger sensitivity to large-scale gradients and to diabatic sources. These observations motivate a term-by-term inspection of the corresponding SBS scalar-variance budgets.

4.2 SBS kinetic-energy budget

Figure 4 shows the signed contribution of each term in the kinetic-energy increment budget (3) as a function of horizontal separation in domain D00 at 5 km altitude (circles denote negative contributions and plus symbols positive contributions). Two ranges can be distinguished.

Mesoscale separations. At the large separations, pressure inhomogeniety (term VI) dominates the balance. This highlights that, in the stratified rotating atmosphere, pressure effects are central in mediating the coupling between large-scale forcing and third-order increment statistics. The non-linear term becomes comparable to the pressure contribution, inheriting the scaling emphasized earlier until subgrid effects start becoming important on smaller scales, at which point we may turn to a nested domain for better resolved statistics. The coherence in scaling is clear in the figure 5 where these term integrated with respect to r are shown over all domains. More specifically, over $r \simeq 3 \times 10^4$–10^6 m, between the buoyancy and Rossby/Rhines length scales, term II is primarily balanced by the signed pressure–inhomogeneity contribution $T_{\mathrm{VI}}(r) \equiv -\langle(\delta u_i)(\alpha^+ + \alpha^-)\,\partial_{X_i}(\delta p)\rangle$ whose scaling in this range is approximately linear. Under horizontal isotropy, $\mathrm{II} \approx (1/r)\,\mathrm{d}[rS_3^u(r)]/\mathrm{d}r$ so to balance linear scaling $\mathrm{II} \propto r$ implies $S_3^u(r) \propto r^2$ over this mesoscale band, consistent with a pressure-forced regime rather than a constant-flux inertial cascade. With the negative pressure gradient covarying along with velocity at the scales larger than 10^5 m, incurring a positive sign on term T_{VI}, the nonlinear transfer can transfer energy upscale. This is also consistent with observations from Cho & Lindborg (2001).

The non-stationarity term (I) is positive across all scales, consistent with the net increase in variability during this heatwave. The inhomogeneity terms (III and VI–IX), which involve derivatives with respect to the midpoint coordinate $\mathbf{X}$, quantify deviations from local homogeneity induced by large-scale organization.

Small separations. At the smallest resolved separations, the transfer term II is mainly balanced by subgrid dissipation/production (X) and by subgrid transport/mixed terms (VII–IX). This range quantifies the transition from resolved transfer to parameterized dissipation in the hybrid-LES closure, and it can be used to assess whether the closure acts as an effective sink of energy at each scale. We have shown this for domain 0 but it remains consistent across domains.

Coriolis effects (XI) peak at separations comparable to deformation/Rhines ranges inferred from figure 2, consistent with the characteristic scales of the rotation-constrained eddies and waves.

4.3 Thermodynamic fields and diabatic imprints

For θ_m, the SBS variance budgets (schematically described in § 3.3) separate transfer-like contributions from direct diabatic injection/removal of variance. In the free troposphere, radiative tendencies and large-scale advection can imprint the variance budget at mesoscale separations, while at smaller separations, turbulent stirring and subgrid mixing dominate. This scale-dependent decomposition is particularly relevant for heatwaves, where persistent clear-sky radiative forcing directly and indirectly modifies temperature variance through its interaction with the large-scale circulation.

4.4 Synthesis with characteristic scales

Figure 2 shows that characteristic scales vary strongly with height, and that the simulated separation range spans regimes where stratification and rotation constraints overlap. The separation range where the structure-function slopes and the SBS budget dominance change is consistent with transitions around the buoyancy/Ozmidov ranges. At the largest separations, proximity to deformation and Rhines scales supports the emergence of rotation-organized variability, which is consistent with the increased relevance of Coriolis-related effects in the SBS budget.

5 Conclusions and outlook

We presented a physical-space, scale-by-scale (SBS) diagnostic framework for momentum and thermodynamic fields in a WRF hybrid-LES simulation of the June 2019 European heatwave. The main points are:

The nested WRF configuration (15 km down to 67 m) provides a single, consistent dataset to examine horizontal structure functions over more than four orders of magnitude in separation.

The SBS kinetic-energy increment budget (3) decomposes the evolution of $(\delta u_i)^2$ into non-stationary effects, scale-to-scale transfer (third-order moment), inhomogeneity/compressibility contributions, pressure-related terms, subgrid transport/dissipation, Coriolis effects and a residual that collects remaining model tendencies.

For the free-tropospheric diagnostics shown here, pressure-related terms dominate at the largest separations, while scale transfer becomes comparable at intermediate separations and is balanced by subgrid dissipation at the smallest separations. Rotation effects are most visible near deformation/Rhines ranges.

Beyond the illustrative 5 km diagnostics reported here, the same methodology can be applied as a function of height and under conditional averaging (day/night, pre-heatwave vs peak-heatwave) to isolate the scale-dependent imprint of diabatic forcing and boundary-layer dynamics. The resulting SBS budgets offer a direct route to connect atmospheric physics parameterizations and external forcing to multi-scale statistics, and they provide a natural bridge between turbulence theory and mesoscale modelling in extreme-event contexts.

Acknowledgements

We acknowledge funding from the French National Research Agency (ANR) under grant ANR-23-CE51-0021 *(LASWATEX)* and access to CRIANN Austral HPC resources.

REFERENCES

Cho, John Y. N. & Lindborg, Erik 2001 Horizontal velocity structure functions in the upper troposphere and lower stratosphere: 1. observations. *Journal of Geophysical Research: Atmospheres* **106** (D10), 10223–10232.

Danaila, L., Krawczynski, J.F., Thiesset, F. & Renou, B. 2012 Yaglom-like equation in axisymmetric anisotropic turbulence. *Physica D: Nonlinear Phenomena* **241** (3), 216–223, special Issue on Small Scale Turbulence.

Göbel, M., Serafin, S. & Rotach, M. W. 2022 Numerically consistent budgets of potential temperature, momentum, and moisture in cartesian coordinates: application to the wrf model. *Geoscientific Model Development* **15** (2), 669–681.

Hersbach, H., Bell, B., Berrisford, P. *et al.* 2020 The ERA5 global reanalysis. *Quarterly Journal of the Royal Meteorological Society* **146** (730), 1999–2049.

Hill, Reginald J. 2001 Equations relating structure functions of all orders. *Journal of Fluid Mechanics* **434** (1), 379–388.

Iacono, M. J., Delamere, J. S., Mlawer, E. J., Shephard, M. W., Clough, S. A. & Collins, W. D. 2008 Radiative forcing by long-lived greenhouse gases: Calculations with the AER radiative transfer models. *Journal of Geophysical Research: Atmospheres* **113** (D13), D13103.

Jiménez, P. A., Dudhia, J., González-Rouco, J. F., Navarro, J., Montávez, J. P. & García-Bustamante, E. 2012 A Revised Scheme for the WRF Surface Layer Formulation. *Monthly Weather Review* **140** (3), 898–918.

Lindborg, Erik & Cho, John Y. N. 2001 Horizontal velocity structure functions in the upper troposphere and lower stratosphere: 2. Theoretical considerations. *Journal of Geophysical Research: Atmospheres* **106** (D10), 10233–10241.

Niu, G.-Y., Yang, Z.-L., Mitchell, K. E., Chen, F., Ek, M. B., Barlage, M., Kumar, A., Manning, K., Niyogi, D., Rosero, E., Tewari, M. & Xia, Y. 2011 The community Noah land surface model with multiparameterization options (Noah-MP): 1. Model description and evaluation with local-scale measurements. *Journal of Geophysical Research: Atmospheres* **116** (D12), D12109.

Skamarock, W. C., Klemp, J. B., Dudhia, J., Gill, D. O., Liu, Z., Berner, J., Wang, W., Powers, J. G., Duda, M. G., Barker, D. M. & Huang, X.-Y. 2019 A Description of the Advanced Research WRF Model Version 4. NCAR Technical Note NCAR/TN-556+STR. National Center for Atmospheric Research, Boulder, CO.

Thompson, G., Field, P. R., Rasmussen, R. M. & Hall, W. D. 2008 Explicit Forecasts of Winter Precipitation Using an Improved Bulk Microphysics Scheme. Part II: Implementation of a New Snow Parameterization. *Monthly Weather Review* **136** (12), 5095–5115.

Xu, Peiqiang, Wang, Lin, Liu, Yuyun, Chen, Wen & Huang, Ping 2020 The record-breaking heat wave of June 2019 in Central Europe. *Atmospheric Science Letters* **21** (4), e964.

Zhang, Xu, Bao, Jian-Wen, Chen, Baode & Grell, Evelyn D. 2018 A Three-Dimensional Scale-Adaptive Turbulent Kinetic Energy Scheme in the WRF-ARW Model. *Monthly Weather Review* **146** (7), 2023 – 2045.

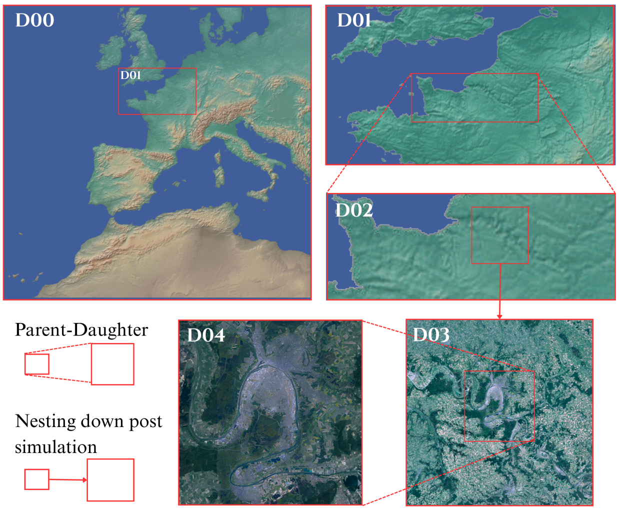

Figure 1. One-way nesting configuration for domains D00–D04. Domains D00 and D01 are forced at the lateral boundaries with ERA5 reanalysis; domains D02 and D04 are forced online by their parent domains during the run; domain D03 is forced by interpolating saved output from domain D02 at its boundaries.

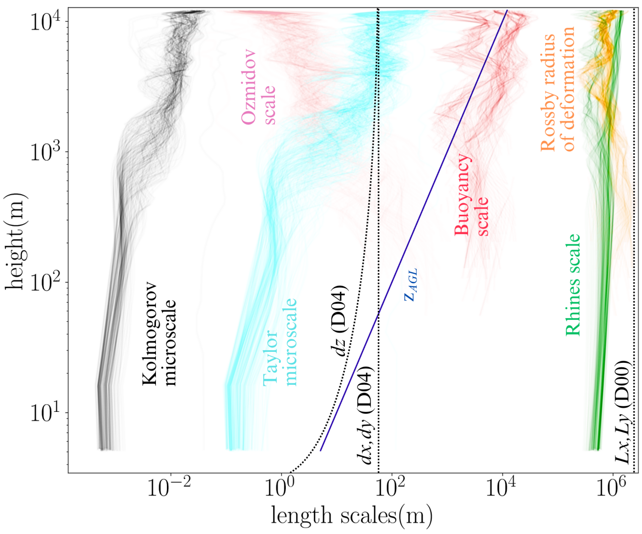

Figure 2. Characteristic atmospheric length scales as a function of the height above ground. Shown are the Kolmogorov microscale (black), Taylor microscale (cyan), Ozmidov scale (pink), Height above ground level (blue), Buoyancy scale (red), Rhines scale (Green) and Rossby radius of deformation (orange). Thin faded lines represent individual realizations, while thicker shading highlights the central tendency. Reference lines indicate model resolution constraints: vertical grid spacing dz, horizontal grid spacing dx, dy for our highest resolution domain $D04$, and domain size L_x, L_y for our largest domain $D00$ to illustrate the range of length scales within simulation bound.

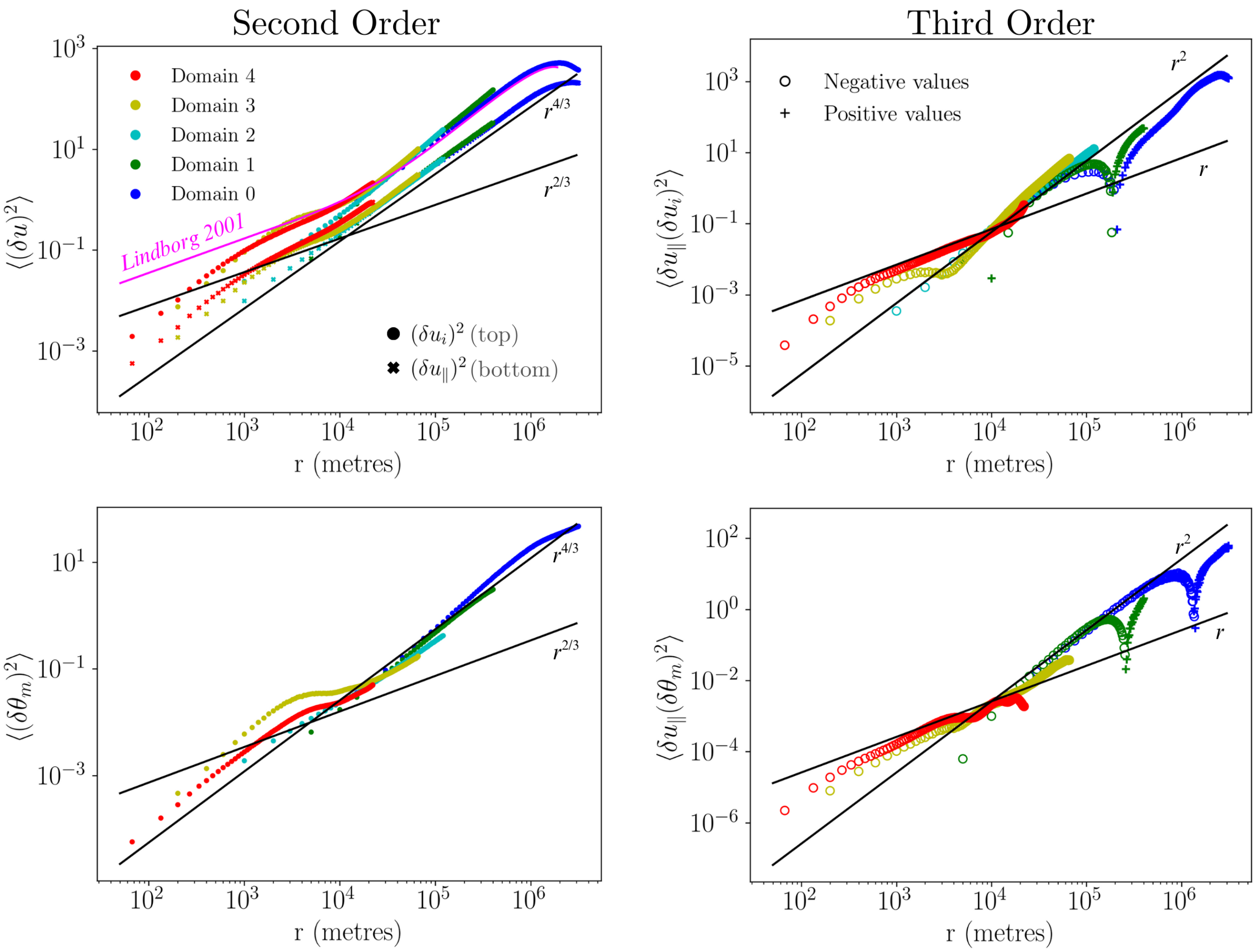

Figure 3. Second-order (left) and third-order (right) horizontal structure functions for resolved velocity (top row), moist potential temperature (bottom row) at 5 km altitude, averaged over the full simulation period.

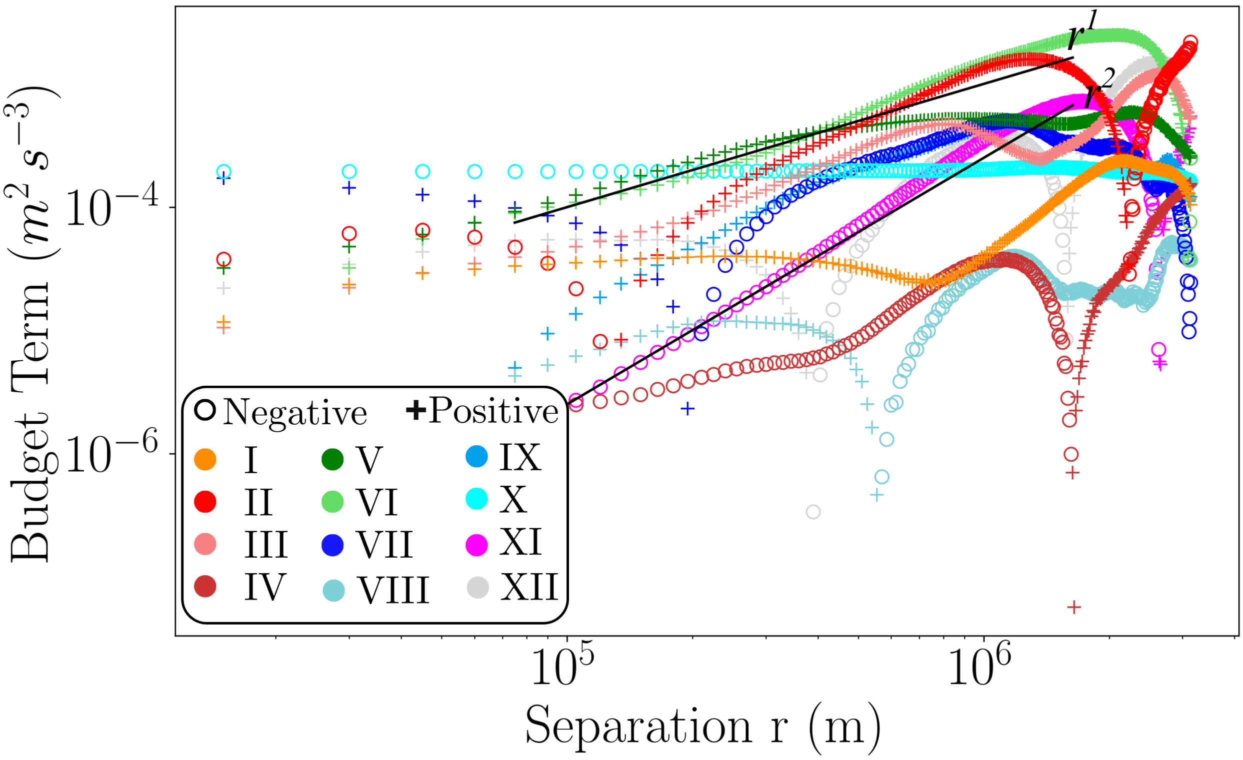

Figure 4. Terms in the SBS kinetic-energy budget (3), averaged over the full simulation period and horizontally at 5 km altitude, in domain D00.

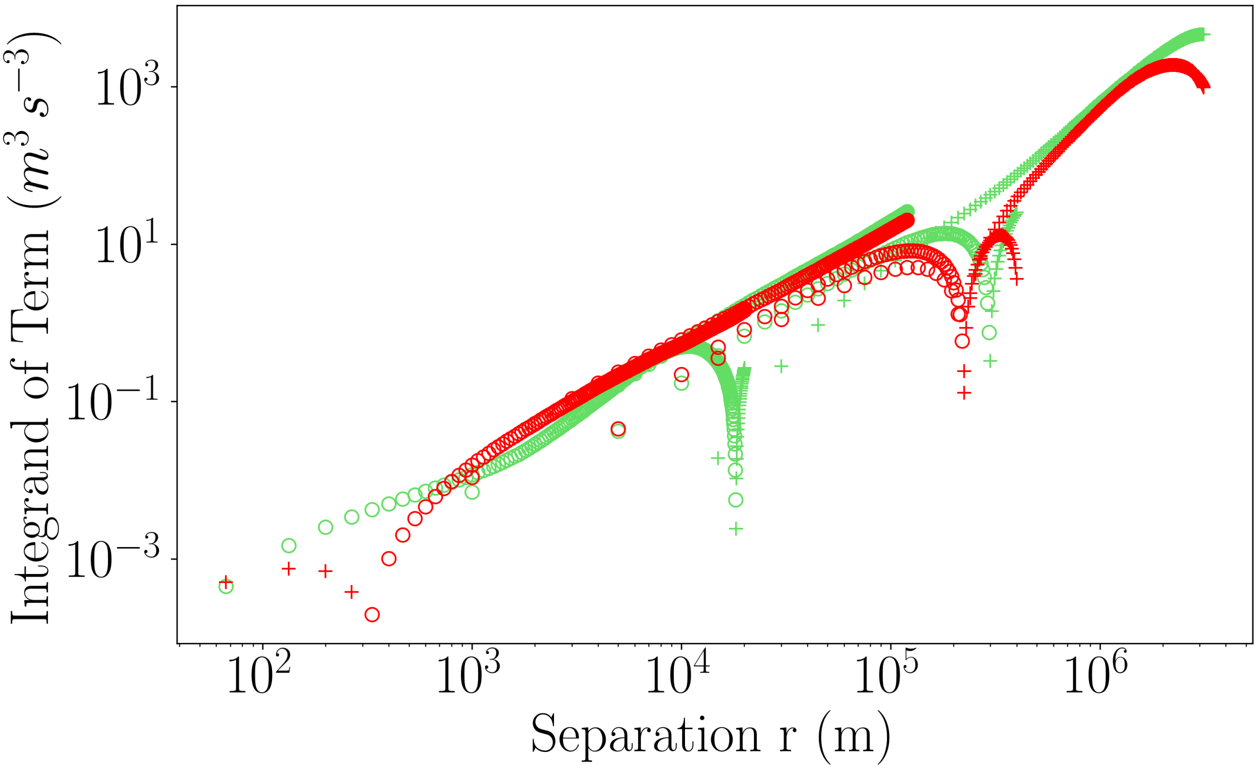

Figure 5. Integrated over r Terms II(red) and VI(green) in the SBS kinetic-energy budget (3), averaged over the full simulation period and horizontally at 5 km altitude, in all Domains.